

Quantum Geometric Friedel Oscillations

Xing-Lei MA,¹ Jinchao Zhao,¹ Bo-Qing Wu,¹ and K. T. Law^{1,*}

¹*Department of Physics, Hong Kong University of Science and Technology, Clear Water Bay, Hong Kong, China*

In conventional Friedel oscillations, the real-space charge density oscillations induced by an impurity are characterized by an oscillation period set by the Fermi momentum. In this work, we show that the conventional theory is incomplete when the Bloch wavefunctions carry nontrivial quantum geometry. We demonstrate that in metals with an isolated (nearly) flat band at the Fermi energy, quantum geometry induces a distinct type of oscillations, which we call the *quantum geometric Friedel oscillations* (QGFOs). The period of the QGFOs is set by the momentum space separation of the quantum metric hot spots of the flat band. The conventional and quantum metric-induced oscillations coexist at low temperatures. At higher temperatures, the conventional Friedel oscillations away from the impurity site are set by the thermal length such that the oscillations can be easily washed out by temperature effects. Remarkably, the QGFOs decay length is set by the quantum metric length which is defined by the integration of the quantum metric of the flat band. As a result, the QGFOs can persist even at temperatures much larger than the bandwidth of the flat band. Moreover, the decay length is independent of temperature for a wide range of temperatures which is a manifestation of the quantum metric protection. In conclusion, we show that the quantum metric induces novel Friedel oscillations. Our work suggests that the measurement of the QGFOs is a powerful way to detect the quantum metric length (which is associated with the integral of the quantum metric) and the quantum metric hot spot separations (which are associated with the distribution of the quantum metric in the momentum space).

Introduction.— The Friedel oscillations are intriguing phenomena caused by the interference of electronic waves induced by charge impurities. The measurements of Friedel oscillations are powerful tools for probing the Fermi surface properties of metals [1]. These charge density oscillations share the same root as other important phenomena such as the RKKY interaction [2–4], the Thomas-Fermi screening [5], and the Kohn-Luttinger mechanism of superconductivity [6]. Conventionally, these real-space oscillations are characterized by a spatial period determined by the Fermi momentum, $2k_F$, and decay away from the impurity site following a power law given the sharpness of the Fermi surface [7]. Consequently, conventional Friedel oscillations are highly susceptible to competing effects that smear the Fermi surface, such as finite temperature and electron-electron interactions [8–11]. Moreover, at finite temperatures, the Friedel oscillation amplitude is suppressed by an exponential decay factor where the decay length is controlled by the thermal length $\xi_T = \hbar v_F / 2\pi k_B T$. This fragility is particularly pronounced in flat-band metals with a quenched Fermi velocity v_F as realized across various experimental platforms [12–17].

The questions are: Are there Friedel oscillations in flat band materials with small v_F ? If the answer is confirmatory, what are the governing length scales of the charge oscillations? This work is devoted to answering the above questions. We show that the conventional Friedel oscillation theory, which ignored the quantum geometric effects [18–48], is incomplete. We point out that the nontrivial Bloch wavefunctions of the flat bands, manifested through the quantum metric and the quantum metric hot spots separations, induce a new type of charge density oscillations which we call the *quantum geomet-*

ric Friedel oscillations (QGFOs). At low temperatures, QGFOs coexist with the conventional Friedel oscillations and give rise to extra oscillating components. At high temperatures, while conventional Friedel oscillations are greatly suppressed by temperature, the QGFOs persist at temperatures even when the thermal energy far exceeds the bandwidth of the flat band. Moreover, the decay length of the QGFOs is determined by the quantum metric length ℓ_{QM} [30, 49–57], which is the integral of the quantum metric of the flat band as defined in Eq. (7).

To be specific, we calculate the charge density of a three band tight-binding model with an impurity site (at $x = 0$) and the details of the model and the calculation methods are given in the End Matter. The band structure of the model and the quantum metric of the flat band $\mathcal{G}^f(k)$ are illustrated in Fig. 1(a). The chemical potential cuts the middle flat band with bandwidth W^f . Normalized charge density oscillations $\delta\rho_{norm}(x)$ near the impurity site and their Fourier spectra $\delta\rho_{norm}(q)$ are depicted in Fig. 1(b) and (c), respectively. The following are the key observations concerning the charge oscillations. First, there are additional oscillating periods at low temperatures ($k_B T \ll W^f$) in Fig. 1(b). The Fourier spectra exhibit sharp features at $2k_F$ as well as q_G , where q_G is the quantum metric hot spots separation defined in Fig. 1(a). In other words, q_G induces new components of Friedel oscillations.

Second, because the QGFOs are rooted in the intrinsic quantum geometry of the Bloch states rather than the sharpness of the Fermi surface, they exhibit remarkable thermodynamic stability. As shown in Fig. 1(b) and (c), while the conventional oscillations are completely washed out by temperature, the QGFOs persist robustly even when the temperature far exceeds the flat-band band-

width. Importantly, as shown in the inset of Fig. 1(b), in the high temperature regime when $k_B T \gg W^f$, the amplitude decay ξ_G of QGFOs is set by the quantum metric length ℓ_{QM} . In Fig. 1(d), upon increasing the temperature, the extracted decay length transitions from a thermal length $\xi_T \propto 1/T$ to a purely quantum-geometric plateau, set by the finite ℓ_{QM} . In sharp contrast, the conventional Friedel oscillations with zero quantum metric length approach zero quickly at finite temperatures [dashed black curve in (d)]. The key connection between q_G and the QGFOs is through the quantum geometric component of the charge susceptibility $\chi_g^f(q)$ in Eq. (5) which peaks at $q = q_G$, as shown in Fig. 1(e). In the following sections, the theory for QGFOs is unfolded.

Theory. — When a local impurity $U_0 \delta(\mathbf{r})$ is introduced in a flat-band metal, the induced density modulations $\delta\rho(\mathbf{r})$ can be related to the static susceptibility function $\chi(\mathbf{q})$ as:

$$\delta\rho(\mathbf{r}) = U_0 \sum_{\mathbf{q}} \chi(\mathbf{q}) e^{i\mathbf{q}\cdot\mathbf{r}}. \quad (1)$$

The susceptibility takes a generic form [58–60] as:

$$\chi(\mathbf{q}) = -\frac{1}{\pi} \Im \left[\frac{1}{N} \sum_{\mathbf{k}} \int_{\omega} f(\omega) \text{Tr} [\mathcal{G}_{\omega}(\mathbf{k} + \mathbf{q}) \mathcal{T}_{\omega} \mathcal{G}_{\omega}(\mathbf{k})] \right], \quad (2)$$

where $\mathcal{T}_{\omega} = \frac{1}{1 - U_0 G_0(\omega)}$ is the \mathcal{T} -matrix, with $G_0(\omega) = \frac{1}{N} \sum_{\mathbf{k}} \mathcal{G}_{\omega}(\mathbf{k})$ the local Green's function, and $\mathcal{G}_{\omega}(\mathbf{k}) = (\omega^+ - H(\mathbf{k}))^{-1}$ with $\omega^+ = \omega + i0^+$. $f(\omega) = \frac{1}{1 + e^{\omega/k_B T}}$ is the Fermi-Dirac distribution at temperature T . For an isolated nearly flat band with $U_0, k_B T \ll \Delta_g$, $\chi(\mathbf{q})$ is dominated by the flat band contribution (see Supplemental Material (SM) [61]), which, after band projection, gives the flat-band susceptibility:

$$\chi^f(\mathbf{q}) = -\frac{1}{\pi} \Im \left[\frac{1}{N} \sum_{\mathbf{k}} \int_{\omega} \frac{f(\omega) \Lambda_{\mathbf{k}+\mathbf{q},\mathbf{k}}^f \tilde{\Lambda}_{\mathbf{k},\mathbf{k}+\mathbf{q}}^f}{(\omega^+ - E_{\mathbf{k}+\mathbf{q}}^f)(\omega^+ - E_{\mathbf{k}}^f)} \right]. \quad (3)$$

Here, the projected form factors $\Lambda_{\mathbf{k},\mathbf{k}'}^f = \langle u_f(\mathbf{k}) | u_f(\mathbf{k}') \rangle$ and $\tilde{\Lambda}_{\mathbf{k},\mathbf{k}'}^f = \langle u_f(\mathbf{k}) | \mathcal{T}_{\omega} | u_f(\mathbf{k}') \rangle$ in the numerator encode the quantum geometry of the flat band. For weak impurities with $U_0 \ll \Delta_g$, $\mathcal{T}_{\omega} \approx \mathcal{I}$ is a reasonable approximation. Physically, the presence of the form factor indicates that during each scattering event, the quantum distance between the final and initial states $d_{\mathbf{k},\mathbf{k}'} \equiv 1 - |\Lambda_{\mathbf{k},\mathbf{k}'}^f|^2$ determines the scattering probability. As a result, the quantum distance fundamentally reshapes the Friedel oscillations. To see this, we rearrange Eq. (3) as:

$$\chi^f(\mathbf{q}) = \chi_c^f(\mathbf{q}) + \chi_g^f(\mathbf{q}), \quad (4)$$

with

$$\chi_c^f(\mathbf{q}) = \frac{1}{N} \sum_{\mathbf{k}} C_{\mathbf{k},\mathbf{q}}^f, \quad \chi_g^f(\mathbf{q}) = -\frac{1}{N} \sum_{\mathbf{k}} C_{\mathbf{k},\mathbf{q}}^f d_{\mathbf{k},\mathbf{k}+\mathbf{q}}. \quad (5)$$

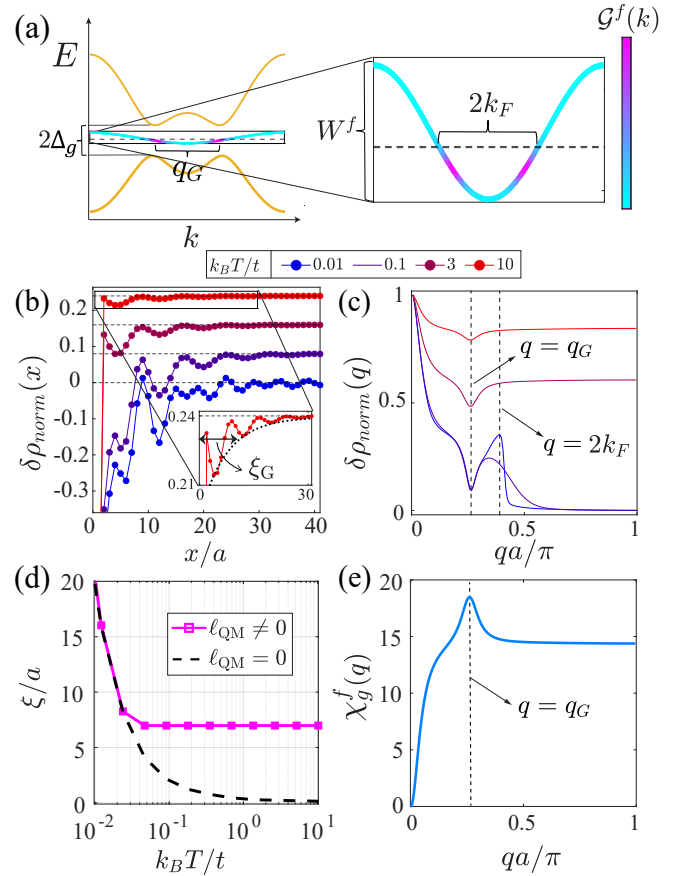


FIG. 1. Emergence and thermodynamic stability of quantum geometric Friedel oscillations (QGFOs). (a) Schematic band structure in a flat-band metal. The color of the central band represents the quantum metric distribution $\mathcal{G}^f(k)$, as zoomed in on the right side. The momentum-space separation between quantum metric hot spots defines the characteristic geometric wavevector q_G . The Fermi level (dashed line) cuts through the flat band, with two Fermi points separated by wavevector $2k_F$. W^f and Δ_g denotes the flat-band bandwidth and the band gap, respectively. (b) Normalized real-space density modulations $\delta\rho_{norm}(x) \equiv \delta\rho(x)/\rho_0$ induced by a local impurity. At low temperatures (blue curve), conventional $2k_F$ oscillations and QGFOs coexist. At high temperatures ($k_B T > W^f$, red curve), the $2k_F$ component is thermally washed out, leaving a pure QGFO response. Curves are vertically offset for clarity. The dashed envelope illustrates the geometric exponential decay ξ_G , which is governed by the quantum metric length ℓ_{QM} . (c) Normalized Fourier spectra of the density modulations across varying temperatures, $\delta\rho_{norm}(q) \equiv \delta\rho(q)/\delta\rho(0)$. Dashed lines mark momenta at which prominent features appear. (d) The long-range spatial decay length ξ extracted across varying temperatures for finite (solid magenta curve) and zero quantum metric length (dashed black curve). (e) Quantum geometric susceptibility in the flat band at temperature $k_B T = 10t$, which exhibits a peak at wavevector q_G . Parameters for (b-d) are: $J = 1$, $t = 10^{-4}J$, $\mu = -1.6t$, $\lambda = 0.02$, $\delta = 0.03$, $\delta' = 5\delta$, $U_0 = 0.01J$.

We introduce χ_c^f and χ_g^f to separate the conventional contribution from the quantum geometric contribution. The shorthand $C_{\mathbf{k},\mathbf{q}}^f \equiv [f(E_{\mathbf{k}+\mathbf{q}}^f) - f(E_{\mathbf{k}}^f)] / (E_{\mathbf{k}+\mathbf{q}}^f - E_{\mathbf{k}}^f)$ is the finite-temperature Lindhard weight. The conventional part in Eq. (5) gives rise to real-space oscillations determined by k_F , with the well-known asymptotic form $\sim -\cos(2k_F r)e^{-r/\xi_T}/r^{d-1}$ in d -dimensions with thermal length $\xi_T = \hbar v_F / 2\pi k_B T$ [9]. In the second, quantum-geometric part, the quantum distance plays a crucial role. Specifically, if $d_{\mathbf{k},\mathbf{k}'}$ peaks (dips) prominently at certain points in $\mathbf{k}-\mathbf{k}'$ plane, e.g., $(\mathbf{k}_g, \mathbf{k}'_g)$, the corresponding wavevector $\mathbf{q}_G = \mathbf{k}'_g - \mathbf{k}_g$ will manifest as oscillatory modes in the local density of states (LDOS), namely, the QGFOs. In Fig. 2(b), we present the quantum distance distribution of the 1D flat-band model, which features two sets of prominent hot lines along $k, k' = \pm q_G/2$ as well as two hot spots at $\pm(q_G/2, -q_G/2)$, which originate from the nearly singular flat band momenta $\pm q_G/2$ with peaking quantum metric in Fig. 2(a). The suppressed overlap (maximal quantum distance) enhances the corresponding component in χ_g^f . At $T = 0$, it will be manifested only if the scattering crosses the Fermi surface, that is, the quantum distance in areas with available particle-hole pairs contributes. Increasing temperature further expands the area accessible to such excitations. And when it includes $(q_G/2, -q_G/2)$, the most strongly suppressed scattering channel, a prominent oscillatory component at q_G occurs, producing the additional oscillations observed in Fig. 1(e). The q_G component strengthens at stronger impurity, and is robustly present irrespective of temperature (see SM [61]).

While Eq. (5) shows that band dispersion and quantum geometry shape the Friedel oscillations on an equal footing, one contribution can dominate the other in certain temperature regimes and spatial ranges. At low temperature $k_B T \ll W^f$, the short-range modulation contains both components, while the conventional Friedel oscillations dominate the long-range tail due to a long thermal length $\xi_T \gg \hbar v_F / (2\pi W^f) \sim a$. On the other hand, the QGFOs become dominant when the temperature increases beyond the bandwidth, i.e., $W^f \ll k_B T \ll \Delta_g$. In this regime, one has $C_{\mathbf{k},\mathbf{q}}^f \simeq -\frac{1}{4k_B T}$, so the quantum geometric susceptibility $\chi_g^f(\mathbf{q})$ becomes proportional to the averaged quantum distance, which is defined as $\bar{D}^f(\mathbf{q}) \equiv \frac{1}{N} \sum_{\mathbf{k}} d_{\mathbf{k},\mathbf{k}+\mathbf{q}}^f$. And it amounts to

$$\chi^f(\mathbf{q}) = -\frac{1}{4k_B T}(1 - \bar{D}^f(\mathbf{q})). \quad (6)$$

The constant term in Eq. (6) represents the conventional part which is uniform in \mathbf{q} -space. It produces a depleted dip at the defect site and no real-space oscillations. Remaining spatial modulations at $k_B T \gg W^f$ are attributed to quantum geometry, i.e., the averaged quantum distance $\bar{D}(\mathbf{q})$. Consequently, peaks and dips in $\bar{D}(\mathbf{q})$ are directly imprinted on the LDOS and generate

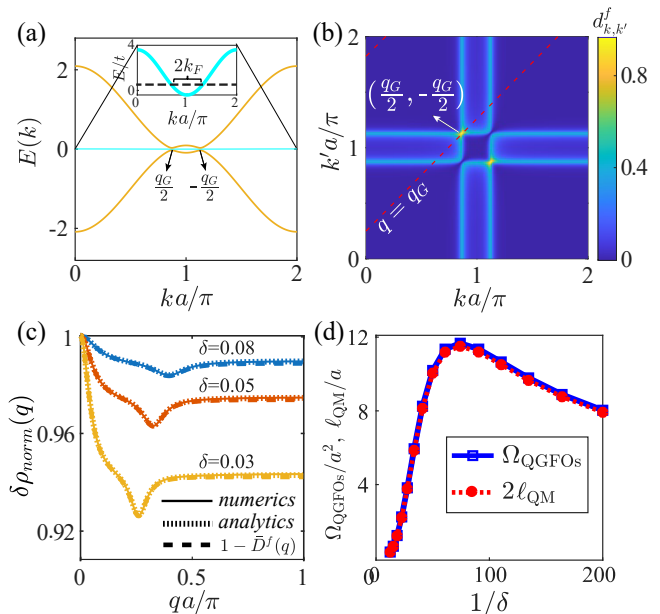


FIG. 2. (a) Band structure of the 1D flat-band model. Inset: Zoom-in of the flat band. The dashed line indicates the Fermi level; $2k_F$ is the zero-temperature scattering wavevector. Parameters are the same as Fig. 1 except $\delta = 0.05$. These parameters are used throughout unless otherwise stated. (b) Quantum distance $d_{\mathbf{k},\mathbf{k}'}$ in the k - k' plane. The red dashed lines mark the cut $q = q_G$ corresponding to the peak of $\bar{D}(q)$. (c) Fourier transform of the LDOS variations $\delta\rho_{\text{norm}}(q)$ for different δ . Solid lines: real-space diagonalization (numerics); dotted lines: full-band formalism in Eq. (2) with $\mathcal{T} = \mathcal{I}$ (analytics). All curves match reasonably well with $1 - \bar{D}^f(q)$. A single impurity $U_0 = t$ is placed at first site; $k_B T = 10t$. (d) Spatial extent Ω_{QGFOs} , scaled quantum metric length $\sqrt{2}l_{\text{QM}}$.

the QGFOs. The relation Eq. (6) is verified in the 1D flat-band model in Fig. 2(c), where the normalized QGFOs spectrum obtained numerically matches well with both the full-band formalism in Eq. (2) and the flat-band contribution in Eq. (6) (under Born approximation). The model parameter δ controls the peaking position in the averaged quantum distance. Consequently, the oscillation period $2\pi/q_G$ shifts with δ . Importantly, since the QGFOs are independent of the Fermi surface, they remain robust against changes in temperature or fillings, in stark contrast to the conventional Friedel oscillations that depend on both (see SM [61]).

As shown in the SM [61], QGFOs take an exponentially decaying form, i.e., $\sim -(A + B \sin(\mathbf{q}_G \cdot \mathbf{r} + \phi))e^{-r/\xi_G}$, where A , B and ϕ are model-dependent constants. In a flat band where kinetic energy is quenched, this spatial confinement is governed not by the vanishing energetic dispersion, but by the analytic pole structure of the band projection operator [55, 57, 62]. The momentum-space variation of the Bloch states restricts how close the complex poles can approach the real axis, rigorously enforcing a geometric floor for the exponential decay length

$\xi_G \geq \lambda \ell_{\text{QM}}$, where λ is an order-1 model-dependent constant. ℓ_{QM} is the quantum metric length [30, 49–55], defined as the Brillouin-zone average of the quantum metric tensor trace:

$$\ell_{\text{QM}} \equiv \frac{V_{\text{cell}}}{(2\pi)^{d_a}} \int \text{Tr}[\mathcal{G}^f(\mathbf{k})] d\mathbf{k}, \quad (7)$$

where V_{cell} is the unit-cell volume. Because this integrated geometry establishes an intrinsic minimum on the spatial spread of localized flat-band modes [63–65], the evanescent tail of the Friedel oscillations is structurally protected from vanishing. As temperature increases and the conventional thermal length ξ_T is suppressed, the spatial extent of the oscillations transitions into a robust, quantum-metric-protected plateau, as observed in Fig. 1(d). Crucially, in the End Matter, we prove that this microscopic geometric bound on individual wave confinement also determines the spatial spread of the density modulations at high temperatures,

$$\Omega_{\text{QGFOs}} = 2a\ell_{\text{QM}}. \quad (8)$$

Here, $\Omega_{\text{QGFOs}} \equiv \langle \mathbf{r}^2 \rangle_{\delta\rho} - \langle \mathbf{r} \rangle_{\delta\rho}^2$ with $\langle \cdots \rangle_{\delta\rho}$ denoting the normalized average weighted by $\delta\rho(\mathbf{r})$ (see End Matter). We validate Eq. (8) in the 1D flat-band model [Fig. 2(d)]. Notably, Eq. (8) holds generically irrespective of specific models or dimensions. For flat Chern metals with Chern number C , the spatial extent is further bounded from below by the topological invariant: $\Omega_{\text{QGFOs}} \geq a^2|C|/\pi$.

The presence of dominant QGFOs is not contingent on extremely high temperature. Given the spatial extent of conventional Friedel oscillations determined by the thermal coherence length ξ_T , they will be suppressed when the coherence length is shorter than the oscillation wavelength, i.e., $\xi_T \lesssim \pi/k_F$. For a parabolic flat band, this suppression occurs at temperatures $k_B T \simeq E_F^f \ll W^f$, where $E_F^f \equiv E_F - E_{\text{min}}^f$ is the Fermi energy measured from the flat-band bottom. Such temperatures are much lower than the bandwidth but high enough to completely smear out the Fermi surface. For realistic flat-band platforms such as magic-angle twisted bilayer graphene, the bandwidth is ~ 10 meV [13], so with a low filling fraction, e.g., $\nu^f \sim 0.1$, QGFOs in such systems—if present—can be predominantly observable at temperatures as low as 10 K. To investigate this regime, let us examine the quantum geometric susceptibility at finite temperature:

$$\chi_g^f(\mathbf{q}) = -\frac{1}{N} \sum_{\mathbf{k}} \int_{\epsilon} f'(\epsilon) C_{\mathbf{k},\mathbf{q},0}^f(\epsilon) d_{\mathbf{k},\mathbf{k}+\mathbf{q}}^f, \quad (9)$$

where $C_{\mathbf{k},\mathbf{q},0}^f(\epsilon)$ is the zero-temperature Lindhard weight with Fermi energy taken at ϵ . Eq. (9) indicates that the dominant quantum geometry arises from the region near the Fermi energy E_F^f within an energy window $\sim T$. Since the states well above and below E_F are thermally frozen, scattering processes within each

frozen sector are suppressed, as are large energy transfers $\Delta E = |E_{\mathbf{k}+\mathbf{q}} - E_{\mathbf{k}}| \gg k_B T$ between two sectors. Contributions of the associated quantum distance to $\chi_g^f(\mathbf{q})$ are suppressed exponentially for the former processes and algebraically $\sim 1/\Delta E$ for the latter. Therefore, for temperature $k_B T \simeq E_F^f$, the relevant quantum geometry is primarily captured by the partially averaged quantum distance

$$\bar{D}_p^f(\mathbf{q}) = \frac{1}{\mathcal{N}} \sum_{E_{\text{min}}^f < E_{\mathbf{k}}^f, E_{\mathbf{k}+\mathbf{q}}^f < \Lambda_c} d_{\mathbf{k},\mathbf{k}+\mathbf{q}}^f, \quad (10)$$

where $\Lambda_c = \kappa k_B T < E_{\text{max}}^f$ (with $\kappa \sim \mathcal{O}(1)$) is an energy cutoff chosen such that $\bar{D}_p^f(\mathbf{q})$ contains all substantial quantum geometric information within the thermally accessible window. The normalization factor $\mathcal{N} = \sum_{E_{\text{min}}^f < E_{\mathbf{k}}^f, E_{\mathbf{k}+\mathbf{q}}^f < \Lambda_c} 1$.

As an example, we examine the 1D flat-band model in this regime and compare the QGFOs before and after altering the quantum geometry of low-energy states. Fixing the flat-band filling fraction $\nu^f \ll 1$ and temperature $k_B T = E_F^f$, the quantum metric hot spots in the flat-band lie within the smeared Fermi surface, i.e., $|E_{k_g}^f - E_F^f| < k_B T$, giving rise to prominent QGFOs with characteristic wavevector q_G [blue curves in Fig. 3(a)]. In contrast, reversing the hopping sign $t \rightarrow -t$ shifts the band bottom by half a BZ while leaving the dispersive bands intact, rendering the quantum metric hot spots thermally inaccessible, i.e., $|E_{k_g}^f - E_F^f| \gg k_B T$. As depicted in the red curves in Fig. 3(a), the oscillation pattern fades after the shift and the spectral dip at q_G disappears, signaling a trivial low-energy quantum geometric structure. Correspondingly, panel (b) confirms that the partially averaged quantum distance exhibits a pronounced peak at $q = q_G$ only before the shift, whereas the shifted case is featurelessly trivial. In conclusion, in the regime $k_B T \simeq E_F^f$, thermal broadening confines the response to a smeared Fermi window, which completely washes out the conventional Friedel oscillations and the QGFOs are governed by $\bar{D}_p^f(\mathbf{q})$. We further corroborate this behavior in a 2D flat-band model in the End Matter.

Discussions.— We have reported quantum geometric Friedel oscillations (QGFOs) in flat-band metals – a real-space response that is independent of the conventional $2k_F$ oscillations. QGFOs are immune to thermal smearing and insensitive to fillings, persisting even when the Fermi surface is completely lost. They originate from the averaged quantum distance $\bar{D}^f(\mathbf{q})$: peaks or dips in $\bar{D}^f(\mathbf{q})$ correspond to suppressed intra-band scattering and directly set the QGFOs wavevector. Notably, such wavevectors are determined by the momentum-space separation of quantum metric hot spots. Concretely speaking, when the flat band nearly touches dispersive bands at a few closely spaced momenta with peaking quantum metric, the quantum distance will exhibit local peaks or

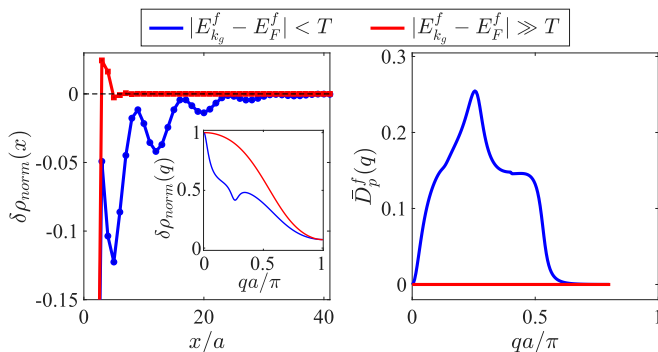


FIG. 3. (a) Comparison of QGFOs with distinct low-energy quantum geometric structures: Quantum metric hot spots living within (Blue curves) versus far above (Red curves) the smeared Fermi surface. Inset: corresponding Fourier spectrum. (b) Partially averaged quantum distance $\bar{D}_p^f(q)$ for the two regimes. Parameters for the blue curves are the same as Fig. 1 except $k_B T = E_F^f = 0.4t$, $U_0 = 10t$, and $\Lambda_c = 3.5k_B T$. The red curve has the same parameters as the blue one except t taking a minus sign.

dips at wavevectors connecting any two of them, generating the QGFOs. Further examples including a two-band model are provided in the SM [61]. Recently, a flat band mimicking the Dice lattice was found experimentally [66], revealing a similar band structure with two nearly touched momenta [67], which suggests a possible platform to detect the QGFOs. Our work establishes QGFOs as the dominant real-space response when kinetic energy is overwhelmed by temperature. Extending this to interacting systems, where correlations may further reshape the spatial screening pattern, is an interesting future direction. The results here also open avenues for exploring thermally robust RKKY interactions, flat band Kondo physics [68], unconventional superconductivity [46], and other correlation-driven phenomena.

Acknowledgment.— We thank Patrick A. Lee, Xilin Feng for inspiring discussions. K. T. L. acknowledges the support of the Ministry of Science and Technology, China, the New Cornerstone Foundation, and the Hong Kong Research Grants Council through Grants No. MOST23SC01-A, No. RFS2021-6S03, No. C6053-23G, No. AoE/P-701/20, AoE/P-604/25R, No. 16309223, No. 16311424 and No. 16300325.

* phlaw@ust.hk

- [1] J. Friedel, *Il Nuovo Cimento* (1955-1965) **7**, 287 (1958).
- [2] M. A. Ruderman and C. Kittel, *Physical Review* **96**, 99 (1954).
- [3] T. Kasuya, *Progress of theoretical physics* **16**, 45 (1956).
- [4] K. Yosida, *Physical Review* **106**, 893 (1957).
- [5] N. W. Ashcroft, N. D. Mermin, *et al.*, *Solid state physics*

- (1976).
- [6] W. Kohn and J. Luttinger, *Physical Review Letters* **15**, 524 (1965).
- [7] G. E. Simion and G. F. Giuliani, *Physical Review B* **72**, 045127 (2005).
- [8] I. Affleck, L. Borda, and H. Saleur, *Physical Review B* **77**, 180404 (2008).
- [9] R. Grassme and P. Bussemer, *Physics Letters A* **175**, 441 (1993).
- [10] F. Cavaliere, N. T. Ziani, F. Negro, and M. Sasseti, *Journal of Physics: Condensed Matter* **26**, 505301 (2014).
- [11] R. Egger and H. Grabert, in *Quantum transport in semiconductor submicron structures* (Springer, 1996) pp. 133–158.
- [12] A. K. Geim and I. V. Grigorieva, *Nature* **499**, 419 (2013).
- [13] Y. Cao, V. Fatemi, S. Fang, K. Watanabe, T. Taniguchi, E. Kaxiras, and P. Jarillo-Herrero, *Nature* **556**, 43 (2018).
- [14] J. Cai, E. Anderson, C. Wang, X. Zhang, X. Liu, W. Holtzmann, Y. Zhang, F. Fan, T. Taniguchi, K. Watanabe, *et al.*, *Nature* **622**, 63 (2023).
- [15] D. Leykam, A. Andreanov, and S. Flach, *Advances in Physics: X* **3**, 1473052 (2018).
- [16] P. M. Neves, J. P. Wakefield, S. Fang, H. Nguyen, L. Ye, and J. G. Checkelsky, *npj Computational Materials* **10**, 39 (2024).
- [17] L. Ye, S. Fang, M. Kang, J. Kaufmann, Y. Lee, C. John, P. M. Neves, S. F. Zhao, J. Denlinger, C. Jozwiak, *et al.*, *Nature Physics* **20**, 610 (2024).
- [18] J. Provost and G. Vallee, *Communications in Mathematical Physics* **76**, 289 (1980).
- [19] R. Resta, *The European Physical Journal B* **79**, 121 (2011).
- [20] P. Törmä, *Physical Review Letters* **131**, 240001 (2023).
- [21] J. Yu, B. A. Bernevig, R. Queiroz, E. Rossi, P. Törmä, and B.-J. Yang, *npj Quantum Materials* **10**, 101 (2025).
- [22] T. Liu, X.-B. Qiang, H.-Z. Lu, and X. Xie, *National Science Review* **12**, nwae334 (2025).
- [23] N. Verma, P. J. Moll, T. Holder, and R. Queiroz, *Nature Reviews Physics*, 1 (2026).
- [24] S. Peotta and P. Törmä, *Nature Communications* **6**, 8944 (2015).
- [25] A. Julku, S. Peotta, T. I. Vanhala, D.-H. Kim, and P. Törmä, *Physical Review Letters* **117**, 045303 (2016).
- [26] X. Hu, T. Hyart, D. I. Pikulin, and E. Rossi, *Physical Review Letters* **123**, 237002 (2019).
- [27] F. Xie, Z. Song, B. Lian, and B. A. Bernevig, *Physical Review Letters* **124**, 167002 (2020).
- [28] J. Herzog-Arbeitman, V. Peri, F. Schindler, S. D. Huber, and B. A. Bernevig, *Physical Review Letters* **128**, 087002 (2022).
- [29] P. Törmä, S. Peotta, and B. A. Bernevig, *Nature Reviews Physics* **4**, 528 (2022).
- [30] S. A. Chen and K. Law, *Physical Review Letters* **132**, 026002 (2024).
- [31] Y. Fang, J. Cano, and S. A. A. Ghorashi, *Physical Review Letters* **133**, 106701 (2024).
- [32] Z. Du, C. Wang, H.-P. Sun, H.-Z. Lu, and X. Xie, *Nature Communications* **12**, 5038 (2021).
- [33] Y. Jiang, T. Holder, and B. Yan, *Reports on Progress in Physics* **88**, 076502 (2025).
- [34] I. Souza, T. Wilkens, and R. M. Martin, *Physical Review B* **62**, 1666 (2000).
- [35] Y. Onishi and L. Fu, *Physical Review Research* **7**, 023158 (2025).

- (2025).
- [36] J. Ahn, G.-Y. Guo, N. Nagaosa, and A. Vishwanath, *Nature Physics* **18**, 290 (2022).
- [37] N. Verma and R. Queiroz, *Proceedings of the National Academy of Sciences* **122**, e2405837122 (2025).
- [38] Z. Han, J. Herzog-Arbeitman, B. A. Bernevig, and S. A. Kivelson, *Physical Review X* **14**, 041004 (2024).
- [39] J.-X. Zhang, W. O. Wang, L. Balents, and L. Savary, *Physical Review Letters* **136**, 176504 (2026).
- [40] E. Rossi, *Current Opinion in Solid State and Materials Science* **25**, 100952 (2021).
- [41] P. Sukhachov, N. H. Aase, K. Mæland, and A. Sudbø, *Physical Review B* **111**, 085143 (2025).
- [42] C.-g. Oh, T. Kitamura, A. Daido, J.-W. Rhim, and Y. Yanase, *Physical Review Research* **8**, 023096 (2026).
- [43] G. Jiang and Y. Barlas, *Physical Review Letters* **131**, 016002 (2023).
- [44] Z.-T. Sun, R.-P. Yu, S. A. Chen, J.-X. Hu, and K. Law, *Quantum Frontiers* **4**, 20 (2025).
- [45] T. Kitamura, A. Daido, and Y. Yanase, *Physical Review Letters* **132**, 036001 (2024).
- [46] G. Shavit and J. Alicea, *Physical Review Letters* **134**, 176001 (2025).
- [47] T. Kitamura, A. Daido, and Y. Yanase, *Physical Review Letters* **132**, 036001 (2024).
- [48] H. Hu, O. Vafek, K. Haule, and B. A. Bernevig, *Physical Review Letters* **136**, 256505 (2026).
- [49] J.-X. Hu, S. A. Chen, and K. T. Law, *Communications Physics* **8**, 20 (2025).
- [50] X. Guo, X. Ma, X. Ying, and K. Law, *Physical Review Letters* **135**, 076601 (2025).
- [51] Z. C. Li, Y. Deng, S. A. Chen, D. K. Efetov, and K. Law, *Physical Review Research* **7**, 023273 (2025).
- [52] C. W. Chau, T. Xiang, S. A. Chen, and K. T. Law, *Quantum metric length as a fundamental length scale in disordered flat band materials* (2026), arXiv:2602.01354 [cond-mat.mes-hall].
- [53] X.-L. Ma, J.-X. Hu, and K. T. Law, *Universal boundary-modes localization from quantum metric length* (2025), arXiv:2509.05114 [cond-mat.mes-hall].
- [54] W.-B. Dai, J. Zhao, S. A. Chen, and K. T. Law, *Quantum metric localization and quantum metric protection* (2026), arXiv:2605.03987 [cond-mat.mes-hall].
- [55] J. Zhao, R. Liu, X.-Y. Song, and K. T. Law, *Quantum metric bound state of light* (2026), arXiv:2606.22479 [cond-mat.mes-hall].
- [56] W. Chen, K. Yang, T. Cao, S.-Z. Lin, J. Yu, and D. Xiao, *Quantum geometric quadrupole of cooper pairs* (2026), arXiv:2605.03133 [cond-mat.supr-con].
- [57] S. Lee, S. H. Lee, and B.-J. Yang, *Physical Review Letters* **137**, 016401 (2026).
- [58] C. Dutreix and M. Katsnelson, *Physical Review B* **93**, 035413 (2016).
- [59] A. Singh, A. Datta, S. K. Das, and V. A. Singh, *Physical Review B* **68**, 235208 (2003).
- [60] W. Chen, X. Zhou, D. Zhang, Y.-Q. Xu, and W.-K. Lou, *Physical Review B* **110**, 165413 (2024).
- [61] See Supplemental Material at URL-will-be-inserted-by-publisher for 1. Analytical form of QGFOs. 2. Interband susceptibilities. 3. Filling dependence of QGFOs. 4. Two-band model. It includes Refs. [69–72].
- [62] Y. Kim, S. Flach, and A. Andreev, *Phys. Rev. B* **113**, 235110 (2026), arXiv:2510.17258 [cond-mat.mes-hall].
- [63] N. Marzari and D. Vanderbilt, *Physical Review B* **56**, 12847 (1997).
- [64] N. Marzari, A. A. Mostofi, J. R. Yates, I. Souza, and D. Vanderbilt, *Reviews of Modern Physics* **84**, 1419 (2012).
- [65] I. Souza, N. Marzari, and D. Vanderbilt, *Physical Review B* **65**, 035109 (2001).
- [66] S. Geng, X. Wang, R. Guo, C. Qiu, F. Chen, Q. Wang, K. Li, P. Hao, H. Liang, Y. Huang, *et al.*, *Nature Communications* (2026).
- [67] J. Zhong, S. Geng, T.-F. Ying, H. Li, and B. T. Zhou, *Ycl electrider as a multi-orbital correlated topological dice lattice system* (2026), arXiv:2509.05958 [cond-mat.mtrl-sci].
- [68] J. G. Checkelsky, B. A. Bernevig, P. Coleman, Q. Si, and S. Paschen, *Nature Reviews Materials* **9**, 509 (2024).
- [69] E. H. Lieb, *Physical Review Letters* **62**, 1201 (1989).
- [70] K. Laubscher, C. S. Weber, M. Hünenberger, H. Schoeller, D. M. Kennes, D. Loss, and J. Klinovaja, *Physical Review B* **108**, 155429 (2023).
- [71] G. Bouzerar, *Physical Review B* **104**, 155151 (2021).
- [72] Y.-D. Luo and M.-F. Yang, *Physical Review B* **110**, 144402 (2024).
- [73] S. Bochner, *Vorlesungen über fouriersche integrale* (Akademische Verlagsgesellschaft, 1932).
- [74] R. Roy, *Physical Review B* **90**, 165139 (2014).

END MATTER

1D Model and Methods.— We consider a 1D three-sublattice model with spin-diagonal Hamiltonian $H^{1D} = \sum_{k,\sigma=\pm} \Psi_{k,\sigma}^\dagger \mathcal{H}_\sigma(k) \Psi_{k,\sigma}$ where $\Psi_{k,\sigma} = (c_{k,\sigma,A}, c_{k,\sigma,B}, c_{k,\sigma,C})^T$ and

$$\mathcal{H}_\sigma(k) = \begin{pmatrix} E_k^f & a_k & b_k \\ a_k^\dagger & E_k^f & 0 \\ b_k^\dagger & 0 & E_k^f \end{pmatrix}, \quad (\text{A1})$$

$$\text{with } a_k = \left[1 + \frac{1+\delta}{2} e^{-ik} + \frac{1+\delta'}{2} e^{ik} \right] J,$$

$$b_k = \lambda J, \quad \text{and } E_k^f = 2t \cos(k) - \mu.$$

Here, we set lattice constant $a = 1$ for simplicity, and μ is the chemical potential. An illustration of the real-space lattice structure is provided in Fig. 4. The model features three bands with one nearly flat band in the middle, as shown in Fig. 2(a). The dispersive bands nearly touch with the flat band at two momenta k_g and $-k_g \pmod{2\pi}$. A zoom-in view of the weakly dispersed flat band is provided in the inset, and we take $0 < t, |\mu| \ll J$ to ensure flatness. The parameters $\lambda, \delta, \delta' \ll 1$ control the band gap $\Delta_g \simeq \sqrt{(\delta' - \delta)^2 (\delta + \delta') / 4 + \lambda^2}$, and δ, δ' determine k_g as well as the quantum geometric texture. When $\delta = \delta'$ the model is inversion symmetric, the quan-

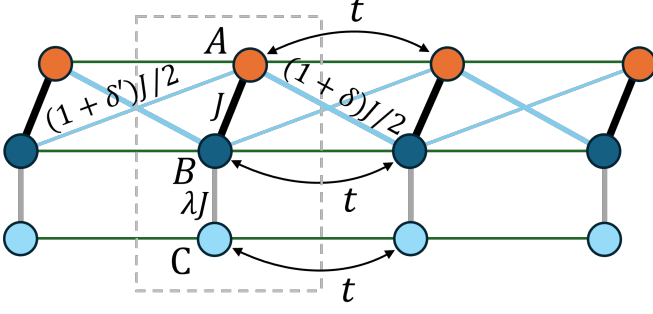


FIG. 4. Real-space lattice and hopping structure of the 1D model. The dashed square denotes an unit cell.

tum distance between Kramers pair vanishes and $\bar{D}^f(q)$ exhibits no local extremum, so no QGFOs appear. For $\delta \neq \delta'$ inversion is broken, yielding a peak in $\bar{D}^f(q)$ at $q_G = 2k_g$ and thus QGFOs. Throughout, time-reversal symmetry is preserved while spatial inversion is broken. Consequently, for a Kramer pair k and $-k$ the Bloch vectors differ, $u_k = u_{-k}^* \neq u_{-k}$, resulting in a finite quantum distance $d_{k,-k} \neq 0$. As shown in Fig. 2(b), the quantum distance exhibits D_2 symmetry from time reversal and exchange, $d_{k_1, k_2} = d_{-k_1, -k_2} = d_{k_2, k_1}$. Two prominent peaks appear at $\pm(k_g, -k_g)$, Scattering across these peaks involves the momentum transfer $q_G = 2k_g$, which manifests as a peak in the averaged quantum distance $\bar{D}^f(q = q_G)$ tunable via δ and δ' , as shown in Fig. 2(c). Hence, a local defect strongly suppresses scattering at $q = q_G$, imprinting spatial oscillations with period $\lambda_G = 2\pi/q_G$. We compute the LDOS variations as $\delta\rho(x) = \sum_{E_{\min}^f < E_i < E_{\max}^f} f_{E_i} |\psi_i(x)|^2 - \rho_0$, and present the normalized quantities $\delta\rho_{norm}(x) = \delta\rho(x)/\rho_0$ and its Fourier transform $\delta\rho_{norm}(q) = \delta\rho(q)/\max[\delta\rho(q)]$ in Figs. 1-3.

2D model with QGFOs. We validate QGFOs in a two-dimensional flat-band model that shares the same 3×3 structure as the 1D Hamiltonian (A1) with the substitu-

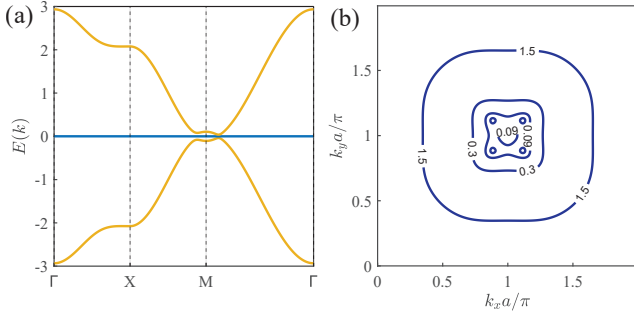


FIG. 5. (a) Band structure of the 2D model. (b) Fermi surface of the third band. Parameters: $J = 1$, $t = 10^{-4}J$, $\delta' = 5\delta$, $\mu = -0.48W^f$ with bandwidth $W^f = 8t$.

tions:

$$\begin{aligned} a_{\mathbf{k}} &= [1 + (1 + \delta)e^{ik_x}/2 + (1 + \delta')e^{-ik_x}/2]J, \\ b_{\mathbf{k}} &= [1 + (1 + \delta)e^{ik_y}/2 + (1 + \delta')e^{-ik_y}/2]J, \end{aligned} \quad (\text{A2})$$

and $E_{\mathbf{k}}^f = 2t[\cos(k_x) + \cos(k_y)] - \mu$, where $0 < t, |\mu| \ll J$ again guarantees a nearly flat band. The band structure is shown as Fig. 5(a), where the flat band in the middle has a parabolic dispersion. It nearly touches the dispersive bands at momenta of two Kramers pairs $(\pm k_g^x, \pm k_g^y)$, as one can tell from the Fermi surface contours shown in panel (b), which leads to quantum metric hot spots at these momenta. Consequently, the quantum distance between momenta of each Kramers pair exhibit a local dip, which further manifests as QGFOs when a local impurity is introduced. Fig. 6(a-c) show the zero-temperature Fourier-space LDOS variations normalized as $\delta\rho_{norm}(\mathbf{q}) = \delta\rho(\mathbf{q})/\max[\delta\rho(\mathbf{q})]$ for three values of δ . The conventional $2k_F$ oscillations (white dashed circles) are independent of δ and disappear when temperature increases to $T = E_F^f$ [panels (d-f)]. The QGFOs (white solid circles) are δ -tunable and survive at $T = E_F^f$. Panels (g-i) plot the partially averaged quantum distance defined in Eq. (10) which we rearrange as $1 - \bar{D}_p(\mathbf{q})$, where the pronounced peaking features coincide with the QGFOs locations in (d-f), confirming that QGFOs at the intermediate temperature regime are governed by the low-energy quantum geometry. Notably, different from the 1D model, the QGFOs in the 2D model persist when both time-reversal and inversion symmetry are present, which means that inversion breaking is not a generic requirements for QGFOs.

Spatial extent of QGFOs and quantum metric length.— Combining Eqs. (1) and (6), the LDOS variation at high temperature is:

$$\delta\rho(\mathbf{r}) = -\frac{U_0}{4TV} \sum_{\mathbf{q}} (1 - \bar{D}^f(\mathbf{q})) e^{i\mathbf{q}\cdot\mathbf{r}}. \quad (\text{A3})$$

Above, for an impurity potential $U_0 \geq 0$, because $(1 - \bar{D}^f(\mathbf{q})) \geq 0$, the Fourier transformation yields a negative definite LDOS variation, $\delta\rho(\mathbf{r}) \leq 0$, according to Bochner's theorem [73]. Thus, the amplitude of $\delta\rho(\mathbf{r})$ generates a probability distribution function $\delta\rho(\mathbf{r})/\sum_{\mathbf{r}} \delta\rho(\mathbf{r})$. Therefore, We define the spatial extent Ω_{QGFOs} of the QGFOs by the variance:

$$\Omega_{\text{QGFOs}} \equiv \frac{\sum_{\mathbf{r}} \mathbf{r}^2 \delta\rho(\mathbf{r})}{\sum_{\mathbf{r}} \delta\rho(\mathbf{r})} - \left(\frac{\sum_{\mathbf{r}} \mathbf{r} \delta\rho(\mathbf{r})}{\sum_{\mathbf{r}} \delta\rho(\mathbf{r})} \right)^2, \quad (\text{A4})$$

with the normalization denominator $\sum_{\mathbf{r}} \delta\rho(\mathbf{r}) = \delta\rho_{\mathbf{q}=0} = -U_0/(4T)$. The first moment vanishes because $\sum_{\mathbf{r}} \mathbf{r} e^{i\mathbf{q}\cdot\mathbf{r}} = -iV\nabla_{\mathbf{q}}\delta_{\mathbf{q},0}$. For the second moment, we use $\sum_{\mathbf{r}} \mathbf{r}^2 e^{i\mathbf{q}\cdot\mathbf{r}} = -V\nabla_{\mathbf{q}}^2\delta_{\mathbf{q},0}$, integrate by parts, and obtain:

$$\sum_{\mathbf{r}} \mathbf{r}^2 \delta\rho(\mathbf{r}) = -\frac{U_0}{4TV} \sum_{\mathbf{k}} 2\text{Tr}[\mathcal{Q}^f(\mathbf{k})], \quad (\text{A5})$$

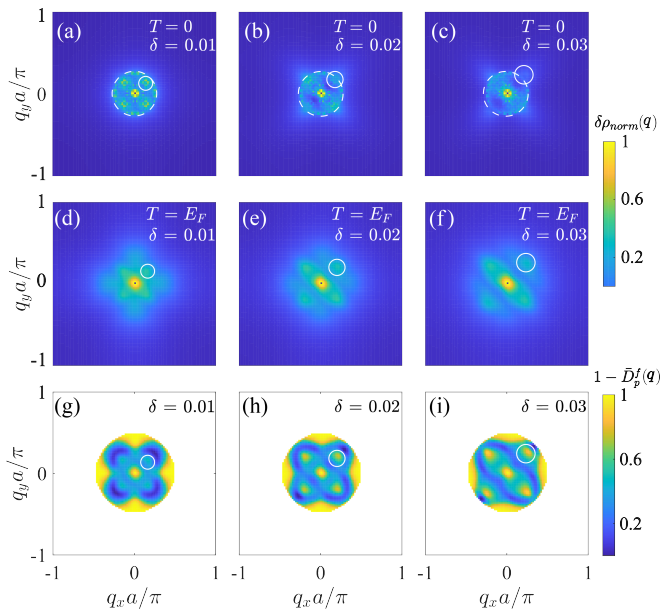


FIG. 6. 2D flat-band QGFOs. (a-c) Normalized LDOS variations in Fourier-space at $T = 0$ for three values of δ . Dashed circles mark the conventional $2k_F$ oscillations; solid circles mark the QGFOs. (d-f) Same as (a-c) at $T = E_F^f$, where the conventional oscillations are washed out and only QGFOs peaks remain. (g-i) Partially averaged quantum distance, rearranged as $1 - \bar{D}_p^f(\mathbf{q})$; the peak locations match the QGFO positions in (d-f). Parameters: $J = 1$, $t = 10^{-4}J$, $\delta' = 5\delta$, $\mu = -0.48W^f$, $E_F^f = 0.02W^f$ with bandwidth $W^f = 8t$, $U_0 = t$, and the cutoff $\Lambda_c = 3.5T$.

where $\mathcal{Q}_{\alpha\beta}(\mathbf{k}) = \langle \partial_{k_\alpha} u_{\mathbf{k}} | (1 - \langle u_{\mathbf{k}} | u_{\mathbf{k}} \rangle) | \partial_{k_\beta} u_{\mathbf{k}} \rangle$ is the quantum geometric tensor. Since $\mathcal{Q}^f = \mathcal{G}^f - \frac{i}{2}\mathcal{B}^f$, its trace is purely the quantum metric. Therefore

$$\Omega_{\text{QGFOs}} = \frac{2}{Na} \sum_{\mathbf{k}} \text{Tr}[\mathcal{G}^f(\mathbf{k})]. \quad (\text{A6})$$

Defining the quantum metric length as Eq. (7), in the thermodynamic limit, we recover $\Omega_{\text{QGFOs}} = 2a \ell_{\text{QM}}$ [Eq. (8)].

In two dimensions, the quantum metric is universally bounded by the Berry curvature \mathcal{B}^f through the inequality [74] $\text{Tr} \mathcal{G}^f(\mathbf{k}) \geq |\mathcal{B}^f(\mathbf{k})|$. Integrating over the BZ yields

$$\frac{1}{N} \sum_{\mathbf{k}} \text{Tr} \mathcal{G}^f(\mathbf{k}) \geq \frac{a^2}{(2\pi)^2} \int |\mathcal{B}^f(\mathbf{k})| d^2k \geq \frac{a^2|C|}{2\pi}, \quad (\text{A7})$$

where C is the Chern number. Hence, for a flat band Chern metal, the spatial extent of QGFOs is bounded from below by the topological invariant:

$$\Omega_{\text{QGFOs}} \geq \frac{|C|}{\pi} a^2. \quad (\text{A8})$$